A Novel B2 Precipitate Gives High Strength and High Impact Toughness to Bcc-Structured Cryogenic Steels

Chen, Qiyuan; Tang, Shuai; Zhang, Weina; Yan, Haile; Sha, Gang; Cao, Guangming; Jin, Shenbao; Wang, Xiaonan; van der Zwaag, Sybrand; More Authors

DOI
10.1002/adfm.202414052

Publication date
2024

Document Version
Final published version

Published in
Advanced Functional Materials

Citation (APA)
Chen, Q., Tang, S., Zhang, W., Yan, H., Sha, G., Cao, G., Jin, S., Wang, X., van der Zwaag, S., & More Authors (2024). A Novel B2 Precipitate Gives High Strength and High Impact Toughness to Bcc-Structured Cryogenic Steels. *Advanced Functional Materials*. https://doi.org/10.1002/adfm.202414052

ADVANCED FUNCTIONAL MATERIALS
www.afm-journal.de

A Novel B2 Precipitate Gives High Strength and High Impact Toughness to Bcc-Structured Cryogenic Steels

Qiyuan Chen, Shuai Tang, Weina Zhang, Haile Yan, Gang Sha, Guangming Cao, Jun Chen, Zhanglong Xie, Shenbao Jin, Xiaonan Wang, Linlin Li, Zhongwu Zhang, Mingxin Huang, Sybrand van der Zwaag,* and Zhenyu Liu**

For decades, solid solution strengthening with up to 9 wt.% Ni has been the only successful strategy to obtain high strength and high impact toughness in bcc-structured (ferritic or tempered martensitic) cryogenic steels. Until now coherent nano-precipitates, an effective strengthening agent at room temperature, cannot be used to improve properties at cryogenic temperatures. Here, a new type of Mo-rich nano-B2 precipitates formed in a 6.5 wt.% Ni steel upon doping with 0.2 wt.% of Mo is reported. These precipitates are not only fully coherent with the matrix but are also shearable at 77 K. A high precipitate number density in excess of 2×10^{24} m^{-3} has been achieved by an industrially feasible process optimization, which brings both the cryogenic strength and impact toughness of the steel to the same levels as those of 9Ni steels. The Mo-rich B2 precipitation strengthening, therefore, opens a new avenue for the design and development of low-cost high-performance cryogenic steels.

1. Introduction

Many key installations in the chemical and energy conversion sector such as tanks for the transport and storage of liquified natural gas (LNG) are running at cryogenic temperatures. Given the dimensions of such installations (volumes up to 270 000 m^3 and plate thicknesses of up to 120 mm), their structural integrity and high resistance to crack initiation and propagation during dynamic loading at ultra-low working temperatures are crucial to ensure safe operation. Therefore, the structural steels require not only high strength but also high impact toughness at cryogenic temperatures. As such, body-centered cubic (bcc)-structured steels (such as ferritic or tempered martensitic steels) containing a high Ni content such as 9Ni steel have been considered to be the best candidates for such applications because of their reasonable combinations of high cryogenic strength and toughness.[1–3] However, further simultaneous improvement of strength and toughness seems to have run into a deadlock because of their trade-off effect.[4] Conventionally, more Ni is added for synergy of strengthening and toughening,[5] but a higher Ni content tends to induce more austenite phase in the steel

---

Q. Chen, S. Tang, W. Zhang, G. Cao, J. Chen, L. Li, Z. Liu
State Key Laboratory of Rolling and Automation
Northeastern University
Shenyang 110819, China
E-mail: zyliu@mail.neu.edu.cn

Q. Chen, X. Wang
School of Iron and Steel
Soochow University
Suzhou 215021, China

H. Yan
School of Materials Science and Engineering
Northeastern University
Shenyang 110819, China

G. Sha, S. Jin
School of Materials Science and Engineering
Herbert Gleiter Institute of Nanoscience
Nanjing University of Science and Technology
Nanjing 210094, China
E-mail: gang.sha@njust.edu.cn

Z. Xie
Nanjing Iron and Steel Co., Ltd.
Nanjing 210035, China

Z. Zhang
Key Laboratory of Superlight Materials and Surface Technology
Ministry of Education
College of Materials Science and Chemical Engineering
Harbin Engineering University
Harbin 150001, China

M. Huang
Department of Mechanical Engineering
University of Hong Kong
Hong Kong 999077, China

S. van der Zwaag
Novel Aerospace Materials Group
Faculty of Aerospace Engineering
Delft University of Technology
Delft 2629HS, Netherlands
E-mail: s.vanderzwaag@tudelft.nl

The ORCID identification number(s) for the author(s) of this article can be found under https://doi.org/10.1002/adfm.202414052

DOI: 10.1002/adfm.202414052

reducing its yield strength,[6] and also carries the risk of deteriorating weldability by magnetic pollution.[7] Therefore, the development of new synergistic strengthening and toughening strategies is highly desirable, in which dislocation slip should be blocked while localized stress concentration should be restrained.

Recently, the formation of coherent B2-type NiAl precipitates with a number density of more than 10^{24} m^{-3} and an average size of ≈2.7 nm has been reported to give martensitic steels with a strength of up to 2.2 GPa and an elongation of 8.2% at room temperature.[8] The NiAl precipitates exploit the chemical ordering effect by high anti-phase boundary energies for effective strengthening.[9] The high anti-phase boundary energy increases the stress required for dislocations to cut through,[10] causing crack initiation to deteriorate impact toughness. Therefore, new promising nano-precipitates have to be fully coherent with the matrix with low anti-phase boundary energies, and massively formed to increase fracture stress according to the Griffith theory. Such new types of precipitates are expected to break the deadlock for simultaneously improving cryogenic strength and impact toughness, but they are yet to be explored in bcc-structured cryogenic steels.

In this work, in order to improve both the strength and impact toughness at cryogenic temperatures and to reduce the required level of Ni alloying, we designed a model steel with a Ni content nearly 30% lower than the customary 9 wt.% Ni, which has the composition of Fe-0.048% C-0.079% Si-0.76% Mn-6.53% Ni and doped it with 0.2% Mo (weight percent), called 6.5NiMo steel. When exploring this steel, we discovered a new type of Mo-rich nano-B2 precipitates, which are not only fully coherent with the matrix but are also cryogenically shearable. We invented a processing route of harnessing their evolutions to generate a high number density of such B2 particles in excess of 2×10^{24} m^{-3}. Amazingly, for such optimal nanoprecipitation the quenched and tempered 6.5NiMo steel reached both strength and impact toughness values at cryogenic temperatures equal to those of industrially optimized 9Ni steels. The Mo-rich nano-B2 precipitates, therefore, can be used to eliminate the trade-off effect on strength and toughness at cryogenic temperatures and to develop a new strategy for the design and development of environment-friendly and less costly high-performance steels for cryogenic industries.

2. Results

2.1. Atomic-Scale Structure Characterization for B2 Nanoprecipitation

Figure 1 shows the transmission electron microscopy (TEM) characterization of B2 nano-precipitates in 6.5NiMo steel (see Figures S1 and S2, Supporting Information for its microstructural characterization). The [100] zone axis high-resolution TEM (HRTEM) image of the tempered martensite revealed the presence of precipitates with an average size of 1–2 nm in a high number density (Figure 1a). By contrast, in the steel without Mo doping (called 6.5Ni steel), very few precipitates with an average size less than 1 nm can be observed (Figure S3a, Supporting Information). The precipitates in 6.5NiMo steel were analyzed using selected area diffraction patterns (SADP) and dark field (DF) images in [100], [110], and [111] zone axes, showing that the superlattice diffraction spots originate from the B2 ordering (Figure S3b–d, Supporting Information). The fast Fourier transform (FFT) patterns of [100] zone axis HRTEM image clearly indicate that the precipitates have an ordered B2 structure (Figure 1b). No sharp B2/matrix interfaces can be observed, indicating that the nano-B2 precipitates are fully coherent with the tempered martensitic matrix. The atomic arrangement of B2 phase was further characterized by [100] zone axis high-angle annular dark-field (HAADF) scanning transmission electron microscopy (STEM). B2 spots can be observed in the FFT pattern of local region (Figure 1c), which is consistent with the HRTEM results. Figure 1d was obtained from Figure 1c by using the inverse FFT to show the typical B2 contrast. Figure 1e shows the atomic columns with periodical changes of brightness intensities along the <001> direction, in good agreement with the B2 ordering.

2.2. Chemical Composition of B2 Nanoprecipitation

To determine the chemical composition of the nano-B2 phase, we performed an atom probe tomography (APT) analysis of the tempered martensitic matrix in 6.5NiMo steel (**Figure** 2a). The APT results show that there are numerous Mo-rich near-spherical precipitates with the size of 1–2 nm in the tempered martensitic matrix, which is consistent with the TEM observations. Proxigram analysis of all near-spherical B2 precipitates indicates that the Mo concentration in the nano-B2 phase is significantly higher than that in the matrix, whereas the Ni concentration in B2 is basically the same as that in the matrix. It is assumed that heavy Mo atoms occupy the body-center positions to form B2 nanoprecipitates, and they correspond to the bright atomic columns marked by white circles in Figure 1d. Although most Mo-rich regions in the matrix are near-spherical, some are elongated (Figure S4a, Supporting Information). We suggest that these elongated Mo-rich regions are caused by some segregation of Mo atoms along dislocations.[11,12] APT also detected obvious Mo, C, Ni, and Mn segregations at high-angle grain boundaries (HAGBs) in the tempered martensite (Figure S4b, Supporting Information). Due to the depletion of surrounding solute atoms as a result of Mo segregation along grain boundaries,[13,14] the number of Mo-rich near-spherical B2 phase adjacent to the grain boundaries is significantly decreased with respect to that in the grain interior.

To understand the effect of Mo on B2 nanoprecipitation, the energy difference $\Delta E_{\text{B2-bcc}}$ between Mo-rich B2 phase and disordered bcc phase was calculated using the first-principles calculations, as shown in Figure 2b. The energy difference reflects the relative stability between B2 phase and disordered bcc matrix. The more negative the $\Delta E_{\text{B2-bcc}}$, the greater the driving force for the precipitation of B2 phase from bcc matrix, which is thermodynamically more favorable for the formation of B2 precipitates.[15,16] The small $\Delta E_{\text{B2-bcc}}$ absolute value of $Fe_{95}Ni_5$ structure shows that the effect of Ni concentration on B2 nanoprecipitation is limited, corresponding to the extremely low number density and small size of B2 precipitates in 6.5Ni steel. Unlike the case for Ni, even a small Mo enrichment greatly reduces $\Delta E_{\text{B2-bcc}}$, which is beneficial to the formation of B2 nanoprecipitates. A trace of Mo promotes the formation of B2 phase in tempered martensite. The number density of Mo-rich nano-B2

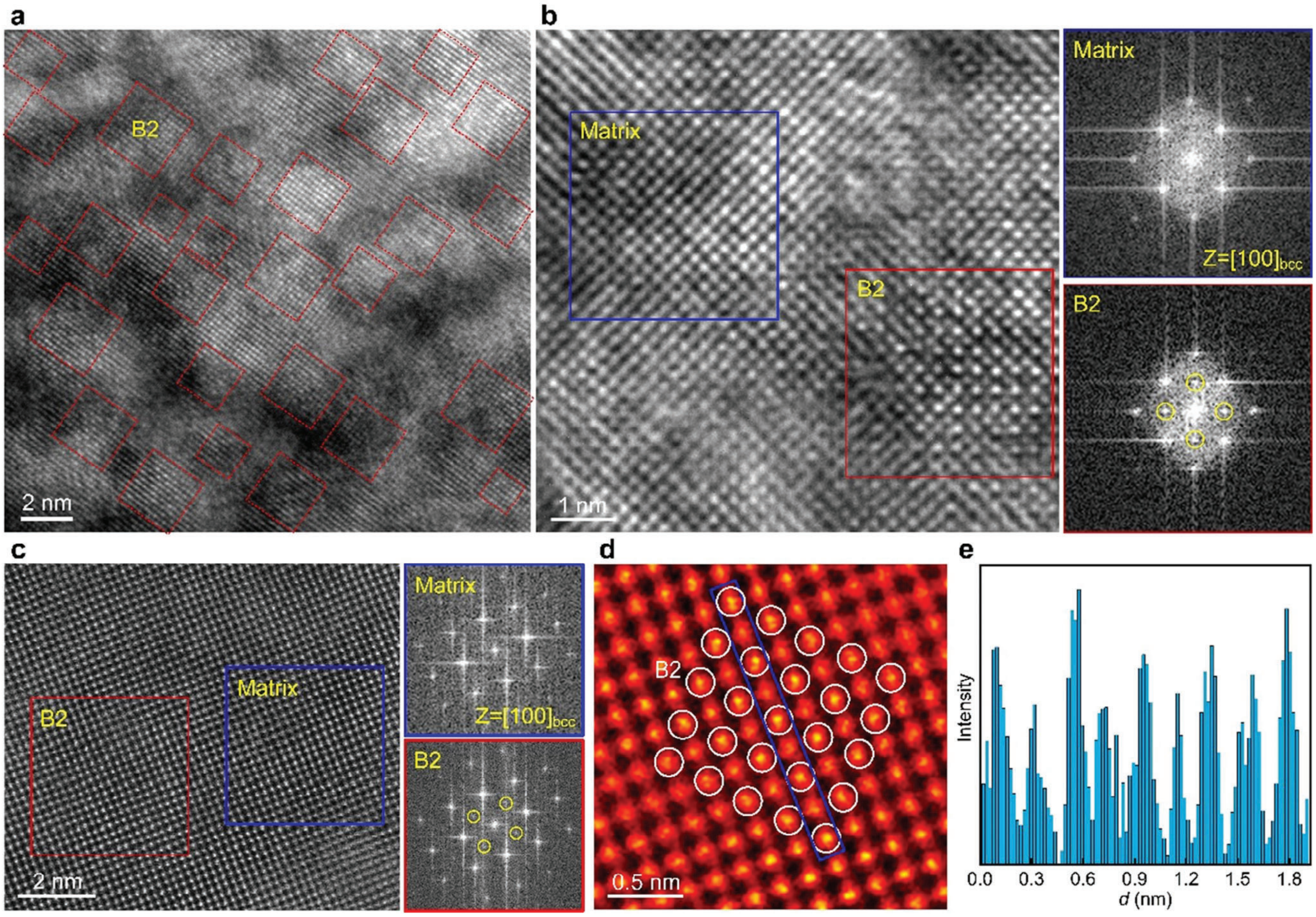

Figure 1. TEM characterization of the tempered martensite in 6.5NiMo steel after tempering treatment (60 min at 863 K). a) [100] zone axis HRTEM image. Red dashed boxes reveal the precipitates. The average size of the precipitates is 1.81 nm. b) [100] zone axis HRTEM image and the corresponding FFT patterns suggesting B2 ordering. c) [100] zone axis HAADF STEM image and the corresponding FFT patterns. The patterns again show the extra B2 spots, besides the sharper spots from bcc phase. d) [100] zone axis inverse FFT image revealing the B2 region. White circles in d highlight some bright atomic columns. e) Intensity line profile along the <001> direction generated from the region in c corresponding to the blue region in d, showing the atomic columns with periodical changes of brightness intensities.

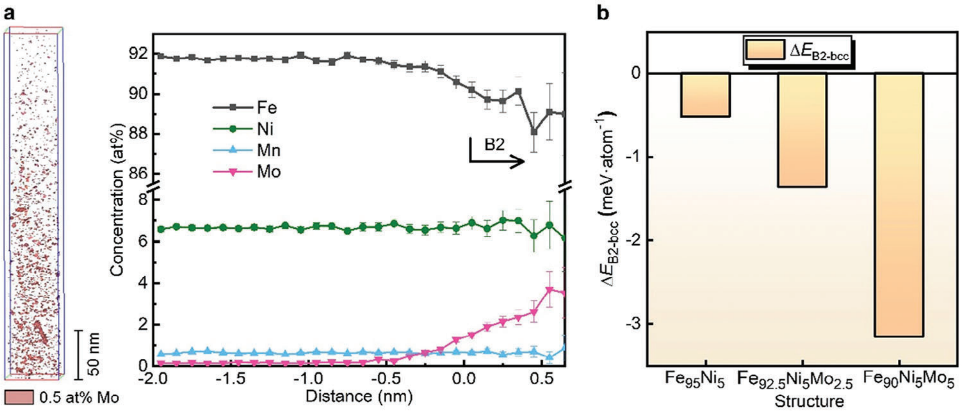

Figure 2. APT characterization of the tempered martensite in 6.5NiMo steel after tempering treatment (60 min at 863 K) and first-principles calculation of the energy gain involved in B2 nanoprecipitation. a) APT reconstruction with nano-B2 precipitates highlighted with iso-concentration surfaces at 0.5 at% Mo and proxigrams across iso-concentration surfaces of the precipitates. b) Energy difference $\Delta E_{\text{B2-bcc}}$ between B2 phase and disordered bcc phase. The negative $\Delta E_{\text{B2-bcc}}$ indicates that B2 precipitation is thermodynamically possible. The Mo enrichment reduces $\Delta E_{\text{B2-bcc}}$ and promotes the B2 precipitation. The number density and size of B2 precipitates in 6.5NiMo steel significantly increase compared to 6.5Ni steel, which is attributed to the promotion of B2 phase formation by Mo doping.

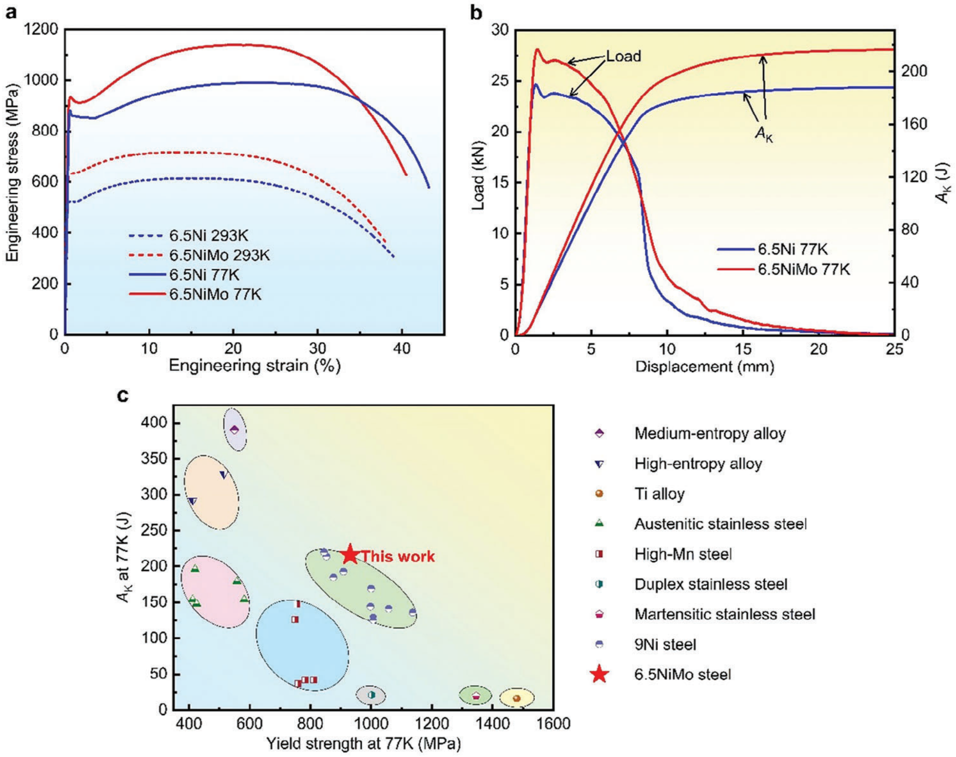

Figure 3. Mechanical properties of 6.5Ni and 6.5NiMo steels after tempering treatment (60 min at 863 K). a) Tensile curves of engineering stress-engineering strain at 293 and 77 K. b) Charpy impact load-displacement curves at 77 K. c) Comparison of mechanical properties of 6.5NiMo steel at 77 K with other cryogenic materials, including 9Ni steels,[20–24] martensitic stainless steels,[25] duplex stainless steels,[26] high-Mn steels,[27,28] austenitic stainless steels,[21,29] Ti alloys,[30] high-entropy alloys,[31] medium-entropy alloys.[32]

precipitates in 6.5NiMo steel was measured to be a very high level of ≈2.6×10^{24} m^{-3} by APT, with the average size of ≈1.73 nm, indicative of a high nucleation rate. Because the Mo-rich nano-B2 precipitates are fully coherent with the matrix, their lower lattice mismatch effectively lowers the elastic strain energy at the B2/matrix interface and promotes extensive uniform nucleation of B2 particles.[8,17] On the other hand, because the growth of B2 particles is controlled by long-range diffusion of Mo, their coarsening is effectively inhibited and the precipitate sizes remain small.[18,19]

2.3. Influence of Mo Doping on the Mechanical Properties

Figure 3a shows the tensile curves of engineering stress-engineering strain both at 293 and 77 K for 6.5Ni and 6.5NiMo steels after 60 min tempering at 863 K. At 293 K, the addition of 0.2 wt.% Mo increased the yield and ultimate tensile strengths by comparable values (110 and 102 MPa respectively), while at 77 K the differences were rather large in favor of the Mo-doped grade (53 and 149 MPa respectively). Figure S5 (Supporting Information) shows the plots of strain hardening rate against true strain of 6.5Ni and 6.5NiMo steels at 293 and 77 K, revealing the better strain hardening capability of 6.5NiMo steel at 77 K. Figure 3b shows the Charpy impact load-displacement curves at 77 K for both steels, which indicate that the impact absorbed energies A_K for 6.5Ni and 6.5NiMo steels were 188 and 216 J, respectively, demonstrating that the Mo doping can improve not only the yield and ultimate tensile strengths but also the impact toughness at 77 K. Mo doping makes the yield strength and impact absorbed energy of 6.5NiMo steel at 77 K comparable to those of conventional 9Ni steels, although Ni content has been reduced by almost 30%. Compared to other cryogenic materials, 6.5NiMo steel has an excellent combination of yield strength and impact-absorbed energy at 77 K (Figure 3c).

2.4. Evolution of Nano-B2 Precipitates with Different Tempering Temperatures

In order to fully understand the precipitation behavior of nano-B2 phase, we studied the evolution of Mo-rich nano-B2 precipitates in 6.5NiMo steel upon 60 min tempering at different temperatures. **Figure** 4a–j shows the typical [100] zone axis SADP and DF images and APT characterization of martensitic matrix after tempering treatments, respectively. Figure 4k,l shows the evolution of number density and size of nano-B2 precipitates with tempering temperatures characterized by APT and TEM. Upon just inter-critical quenching, the number density of nano-B2 precipitates in the martensitic matrix was measured to be $2.47–3.22 \times 10^{23}$ m^{-3}, and their average size was in the range of 1.38–1.42 nm. Upon the tempering treatment, both number density and particle size changed in a parabolic manner with the tempering temperature, reaching their plateaus at 863 K

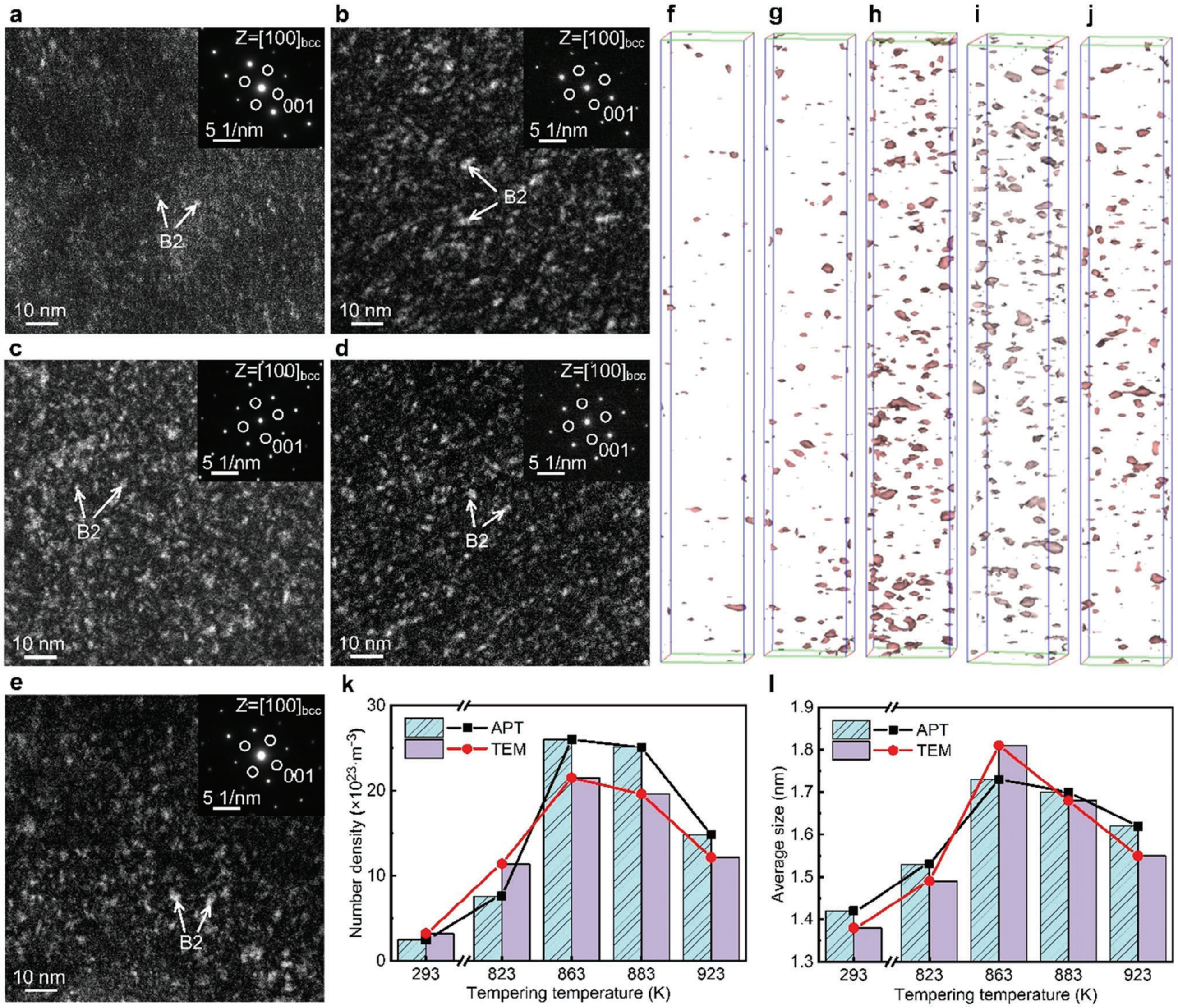

Figure 4. Evolution of nano-B2 precipitates in the martensitic matrix of 6.5NiMo steel with tempering temperatures. a–e) [100] zone axis SADP and DF images of the inter-critically quenched (untempered) and tempered (60 min at 823, 863, 883, and 923 K) samples, respectively. White circles in SADP of a–e represent extra superlattice diffraction spots, and the corresponding DF images reveal the precipitates. f–j) APT reconstructions of the untempered and tempered (60 min at 823, 863, 883, and 923 K) samples, respectively. The size of all boxes in f–j are 20 nm × 20 nm × 150 nm. B2 precipitates are highlighted with iso-concentration surfaces at 0.5 at% Mo. k. Number density of B2 precipitates is determined by APT and TEM. l. The average size of B2 precipitates is determined by APT and TEM.

with a maximum number density of 2.15–2.6 × 10^{24} m^{-3} and an average size in the range of 1.73–1.81 nm for the Mo-doped steel. It should be noted that the number densities and particle sizes determined by APT and TEM are in good agreement, indicating that the nucleation is very homogeneous and independent of local defects or local composition fluctuations. Figure S6 (Supporting Information) shows the proxigram analysis of B2 precipitates formed at different tempering temperatures, which indicates that Mo concentration in B2 precipitates is significantly higher than that in the matrix, whereas the Ni concentration in B2 is basically the same as that in the matrix, implying that the precipitation of B2 phase involves long-range diffusion of Mo.

Immediately after quenching, the Mo atoms should be uniformly distributed in the fresh martensitic matrix corresponding to the solid solution stage reached during austenization prior to quenching. During tempering, the Mo-rich nano-B2 phase begins to nucleate and grow controlled by long-range diffusion. Considering that the diffusion coefficients of Fe, Ni and Mo at 823 K are lower than those at 863 K (Table S1, Supporting Information),[33–35] a lower atomic mobility may inhibit the nucleation and growth of B2 nanoprecipitation at tempering temperatures lower than 863 K. In contrast, the higher atomic mobility at 863 K has led to easier formation of nano-B2 precipitates with a lower free-energy state in the matrix,[36] resulting in higher number density and larger average size. When the tempering

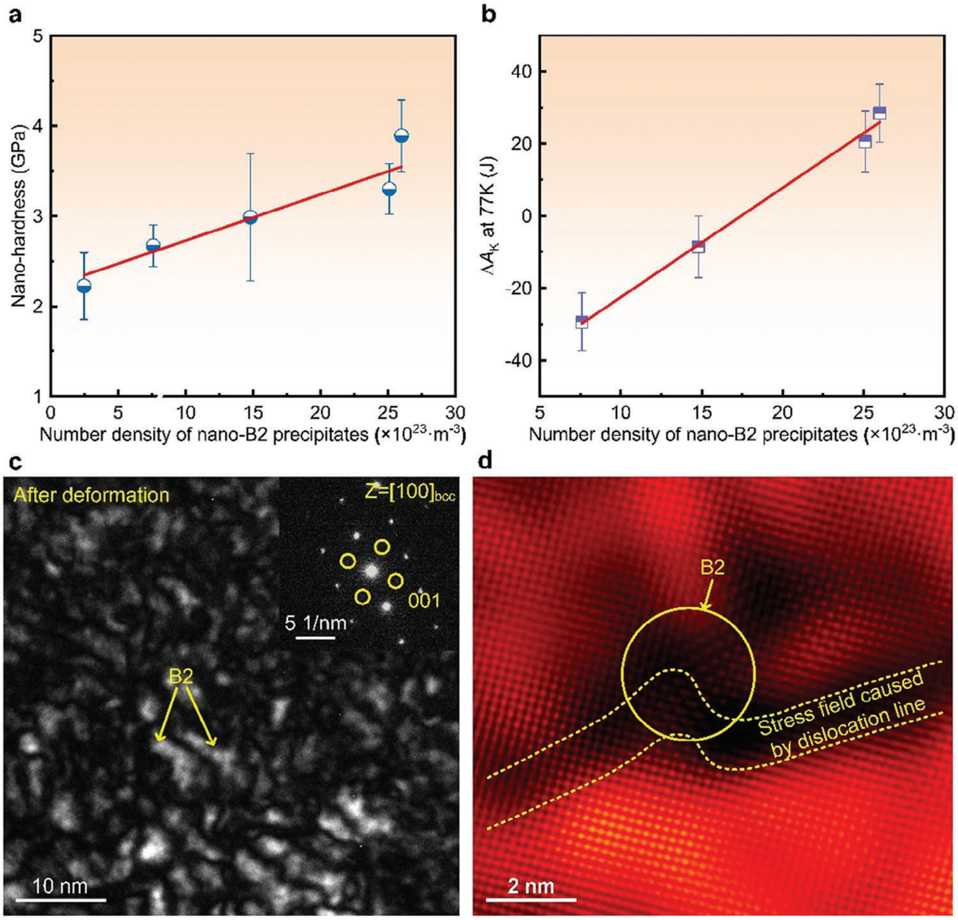

Figure 5. Influence of number density of Mo-rich nano-B2 precipitates on mechanical properties and interaction between Mo-rich nano-B2 phase and dislocations. a) Changes in nano-hardness of martensitic matrix with number density of Mo-rich nano-B2 precipitates in 6.5NiMo steel. b) Variation of ΔA_K at 77 K with number density of Mo-rich nano-B2 precipitates in 6.5NiMo steel. c) [100] zone axis SADP and DF image of the tempered martensite at the vicinity of the impact fracture with the tempering temperature of 863 K, revealing that most of the precipitates are obviously elongated after deformation. d) [100] zone axis HRTEM image of the tempered martensite at the vicinity of the impact fracture with the tempering temperature of 863 K, showing a slight bending of the dislocation cut into the precipitates.

temperatures are higher than 863 K, although the diffusion of Fe, Ni and Mo becomes easier (Table S1, Supporting Information), B2 phase tends to disorder to reduce its chemical driving force for precipitation. As a result, some B2 precipitates get dissolved, leading to the decrease in both the number density and size. A similar behavior has been reported in the study of isothermal ω phase precipitation in metastable Ti alloys.[37,38]

2.5. Influence of Number Density of B2 Nanoprecipitates on Mechanical Properties

Figure 5a shows the variation of nano-hardness of the martensitic matrix for 6.5NiMo steel as a function of the number density of Mo-rich nano-B2 precipitates. The nano-hardness gradually increases with increasing number density of nano-B2 precipitates. Although the increase in recovery degree of the martensitic matrix and the decrease in Ni concentration in the martensitic matrix (Figure S6, Supporting Information) should lead to a continuous decrease of nano-hardness with increasing tempering temperature, a peak nano-hardness is achieved at 863 K due to the highest number density for Mo-rich nano-B2 precipitates. The observation demonstrates that Mo-rich nano-B2 precipitates have a significant strengthening effect on 6.5NiMo steel.

To reveal the influence of the number density of nano-B2 precipitates on impact toughness at 77 K, we introduced the increment of impact absorbed energy, ΔA_K, at 77 K for 6.5NiMo steel relative to 6.5Ni steel at the same tempering temperature. As shown in Figures S7 to S9 (Supporting Information), the volume fraction, size, and distribution characteristics of the reversed austenite in both steels tempered at the same temperature are almost the same, while ΔA_K changes abruptly with tempering temperatures, indicating that reversed austenite should not be held responsible for the change in ΔA_K. By excluding the toughening effect to come from the reversed austenite, ΔA_K should come from the toughening effect of Mo-rich nano-B2 precipitates. Figure S10 (Supporting Information) shows the impact fracture morphologies of 6.5Ni and 6.5NiMo steels with different tempering temperatures, revealing that the fracture modes of both untempered steels are cleavage fractures, whereas those after tempering change to transgranular ductile fractures. These results indicate that the Mo-rich nano-B2 precipitates do not induce crack initiation and cleavage fracture found previously for B2 reinforced steels reported in the literature.[39,40] For the samples with transgranular ductile fractures, ΔA_K increases monotonically with the increasing number density of Mo-rich nano-B2 precipitates in 6.5NiMo steel (Figure 5b), demonstrating that Mo-rich nano-B2 precipitation plays a decisive role in toughening the Mo-doped steel at cryogenic temperatures.

2.6. Interaction Between Dislocations and B2 Nanoprecipitates

To elucidate the interaction between moving dislocations and Mo-rich nano-B2 precipitates during impact loading at 77 K, the deformed microstructure of the 6.5NiMo steel at the vicinity of the impact fracture was characterized by HRTEM. The [100] zone axis SADP and DF image in Figure 5c shows that most of the precipitates are elongated and have lost their original equiaxed spherical shape. The shape change clearly indicates that dislocations have cut through these precipitates, causing them to undergo plastic deformation together with the matrix. The HRTEM image in Figure 5d shows additional evidence that the dislocations do cut through B2 precipitates. Figure S11 (Supporting Information) shows the bright field image of a dislocation line, which corresponds to the dark contrast in Figure 5d caused by the stress field of the dislocation line. The displacement distance of dislocations inside B2 should be slightly smaller than that in the surrounding matrix,[41] resulting in the slight bending of dislocations.

3. Discussion and Conclusion

All the above evidences indicate that the novel B2 nano-precipitates are responsible for the synergistic strengthening and toughening of the steel at cryogenic temperatures. The strengthening effect of nano-B2 precipitates generally originates from the coherency hardening by elastic coherency strain between them and the matrix,[42] the order hardening by the formation of anti-phase boundaries through dislocation shearing,[43] and the modulus hardening by modulus difference between them and the matrix.[44] The strengthening effect of Mo-rich nano-B2 precipitates is no exception, whereas their effect on cryogenic impact toughness is quite different from that of NiAl-B2 precipitates. Therefore, we further clarified the underlying toughening mechanisms by the novel B2 nano-precipitates at cryogenic temperatures. Figure S12 (Supporting Information) shows the TEM bright field images of dislocation configurations in the impact samples after fracture. The higher dislocation density in tempered martensitic steels induces a significant multiplication and accumulation of dislocations during deformation, contributing to continuous strain hardening. With the increase of deformation, the interaction between dislocations is enhanced, and they tend to entangle and rearrange with each other, leading to the formation of dislocation networks and dislocation cells. In the later stage of deformation, the dislocation density gradually saturates, and microcracks are initiated when local stress concentration reaches the critical fracture stress. The propagation and interconnection of these microcracks may ultimately lead to failure fracture. Figure S13 (Supporting Information) schematically illustrates the interactions between nano-B2 precipitates and dislocations in the Mo-containing steel grade during impact loading. When dislocations in tempered martensitic matrix encounter B2 precipitates at the initial stage of deformation, they may reach the B2/matrix interface. Due to the coherency between B2 particles and the matrix, the slip of dislocations is barely hindered by the interfacial lattice mismatch, resulting in insignificant dislocation pile-ups and less strain accumulation for crack initiation.[8] The B2 particles are then cut through by the dislocations, leaving anti-phase boundaries inside the precipitates.[45] Using first-principles calculation (see details in Methods), the anti-phase boundary energy γ_{apb} of Mo-rich B2 phase is assessed to be 0.12 J m^{-2}, which is significantly lower than that for the average γ_{apb} of NiAl-B2 phase (0.5 J m^{-2}),[9] showing better plastic deformation capacity and shearability at cryogenic temperatures to suppress cracking as dislocations cutting through nano-B2 particles. With the continuous deformation of matrix, B2 particles can be cut through by dislocations in the matrix along the slip direction, leaving several anti-phase boundaries inside the B2 particles, and their morphologies change from near-spherical to elongated. Finally, and most importantly, because these B2 precipitates in the Mo-doped steel rarely generate cracks during deformation, their resistance against dislocation slip enhances the load bearing capacity to increase the energy dissipation by forming anti-phase boundaries during impact loading, resulting in improved cryogenic toughness.

Assuming that the additional work of the moving dislocations cutting through the B2 precipitates is all to form the anti-phase boundaries, the toughening increment ΔA_K by novel B2 nano-precipitates can be evaluated from the following empirical formula. For order hardening by B2 precipitates, the stress increment can be estimated by Equation (1).[43]

$$\Delta\tau_{\text{order}} = \left(\frac{M\gamma_{\text{apb}}^{3/2}}{b}\right)\left(\frac{4rf}{\pi T}\right)^{1/2} \tag{1}$$

where, $M \approx 3$ for the Taylor factor, r for the average radius of Mo-rich nano-B2 precipitates, b for the Burger vector of the dislocation, γ_{apb} the anti-phase boundary energy for B2 phase, $T = Gb^2/2$ for the dislocation line tension, $f = (4/3)\pi nr^3$ for the volume fraction of precipitates, and n for the number density of Mo-rich nano-B2 precipitates. The work for forming anti-phase boundaries can be estimated by Equation (2).

$$\Delta A_K = \left(\frac{M\gamma_{\text{apb}}^{3/2}}{b}\right)\left(\frac{4rf}{\pi T}\right)^{1/2} b\left(\frac{4\pi r^3}{3f}\right)^{1/3} 2r\frac{3f}{4\pi r^3} \tag{2}$$

since M, b, γ_{apb}, and T are constant, Equation (2) can be written as Equation (3).

$$\Delta A_K = kf^{7/6}r^{-1/2} \tag{3}$$

where, $k = \left(\frac{M\gamma_{\text{apb}}^{3/2}}{b}\right)\left(\frac{4}{\pi T}\right)^{1/2} 2b\left(\frac{3}{4\pi}\right)^{2/3}$. It is deduced from the empirical formula that ΔA_K is proportional to $f^{7/6}r^{-1/2}$, which is well confirmed by the results in Figure S14 (Supporting Information).

Given the high number density of the B2 precipitates in the Mo-doped steel, a large number of precipitates will be cut, resulting in more extensive toughening.

In conclusion, novel Mo-rich B2 nanoprecipitation provides a new non-solid solution alloying strategy for breaking the cryogenic strength-toughness trade-off effect. Mo-rich nano-B2 precipitates are fully coherent with the matrix, and have the capability of undergoing plastic shear deformation even at cryogenic temperatures. The optimization for the number density and size of Mo-rich nano-B2 precipitates can be achieved by optimizing the tempering treatment, which efficiently improves both the strength and impact toughness at 77 K for Ni-containing cryogenic steels. We have conducted industrial production trials and successfully manufactured 6–50 mm thick 6.5NiMo plates to replace conventional 9Ni steel in the construction of 50 000 m^3 cryogenic tanks (Figure S15, Supporting Information). This success demonstrated the feasibility of the strengthening and toughening strategy on an industrial scale. This new strategy illustrated by this research is of significance in developing other high-performance cryogenic and non-cryogenic steels while reducing the addition of expensive and scarce elements such as Ni.

4. Experimental Section

Sample Preparation: Two 100 kg steel ingots of 6.5Ni and 6.5NiMo steels were prepared by standard vacuum induction melting. The chemical compositions of both steels were Fe-0.048% C-0.051% Si-0.78% Mn-6.47% Ni (weight percent) and Fe-0.048% C-0.079% Si-0.76% Mn-6.53% Ni-0.2% Mo (weight percent), respectively. The ingots were homogenized at 1473 K for 120 min, hot rolled in austenitic recrystallization regimes into 15 mm in thickness, and fast cooled to room temperature (also called online direct quenching). The reduction in finishing rolling was ≈68% and the final rolling temperature was 1093 K. The hot rolled steel plates were reheated to 973 K and held for 40 min, and water-quenched to room temperature (also called inter-critical quenching). The inter-critically quenched steel plates were tempered at 823, 863, 883, and 923 K for 60 min, respectively.

Mechanical Property Measurement: The longitudinal tensile specimens with a diameter of 7 mm and the transverse Charpy impact specimens with a size of 10 mm × 10 mm × 55 mm were machined from the tempered steel plates. The tensile tests were carried out at 293 and 77 K by using a CMT5000-SANS machine with a crosshead speed of 2 mm min^{-1} and a gauge length of 25 mm. The Charpy impact tests were carried out at 77 K in a liquid nitrogen environment by using an Instron MPX series pendulum impact tester. The fracture morphology of Charpy impact specimens was observed by using a Zeiss Ultra-55 scanning electron microscopy (SEM). The nano-hardness was measured using a Hysitron Triboindenter with a Berkovich indenter with a peak load of 2000 µN.

Microstructural Characterization: The microstructure was characterized using a Thermoscientific Apreo2C SEM equipped with Oxford Symmetry electron back scatter diffraction (EBSD). The acceleration voltage was 15 kV, and the step size was 50 nm. The volume fraction of reversed austenite was measured by using a D/max2400 X-ray diffractometer (XRD), equipped with Cu Kα radiations. The step size was 4° min^{-1}, and the degree of 2θ was 40–100°. The samples for EBSD and XRD analysis were prepared through grinding and electropolishing with an electrolyte of 12.5% perchloric acid and 87.5% alcohol at 293 K. The volume fraction V_γ of reversed austenite was calculated from the integrated intensities of $(200)_{fcc}$, $(220)_{fcc}$, $(311)_{fcc}$, $(200)_{bcc}$, and $(211)_{bcc}$ diffraction peaks.[46]

TEM Characterization: The TEM characterization was performed by using a Tecnai G^2 F20 TEM. The samples for TEM characterization were prepared by grounding the steel plate into 50 µm in thickness and electropolishing at 248 K. The atomic-resolution HAADF STEM characterization was performed by using an aberration-corrected JEOL JEM-ARM200F STEM operated at 200 kV. The aberration-corrected STEM sample was prepared by a Lift-out technique using an FEI Helios NanoLab 600i focused ion beam SEM.

APT Characterization: The APT characterization was performed by using a Cameca LEAP 4000X SI instrument at 40 K. The pulse UV laser energy was 50 pJ, the pulse repetition rate was 200 kHz, and the target evaporation rate was 1.0% per pulse. The samples for APT analysis were prepared by a two-step electropolishing procedure. The first step used an electrolyte of 25% perchloric acid in acetic acid at 15 V at 293 K and the second step used an electrolyte of 4% perchloric acid in 2-butoxethynal at 20 V. A commercial software Cameca IVAS 3.6.12 was used to reconstruct the APT data.

First-Principles Calculation: The total energy was performed using the exact muffin-tin orbitals (EMTO) method based on the density functional theory (DFT). The chemical disorder on the atomic scale was taken into account using the coherent potential approximation (CPA).[47–50] The generalized gradient approximation (GGA) was selected as the exchange-correlation density functional and the total energy was obtained from the full Perdew–Burke–Ernzerhof (PBE) scheme.[51] The scalar-relativistic approximation and soft-core scheme were used. The structure of bcc and B2 with the ferromagnetic state was calculated. Likewise, the Brillouin zone integration was performed on 21 × 21 × 21 k points mesh. The energy difference $\Delta E_{B2\text{-}bcc}$ between B2 and bcc was obtained by the energy of the final state minus the energy of the first initial state.

The anti-phase boundary energy γ_{apb} for B2 phase was performed using the DFT as implemented in the Vienna ab initio Simulation Package (VASP).[52] The projected augmented wave (PAW) potentials and the GGA of PBE for exchange-correlation were applied.[53–55] The conjugate-gradient algorithm was used to full relax all atomic positions, cell shapes, and cell volumes to achieve the minimum total energy of the systems until the average force on each atom was less than 0.03 eV $atom^{-1}$. The cut-off energy for plane wave expansion was 350 eV for all models. The total energy and force convergences were 10^{-6} eV $atom^{-1}$.[56] The gamma-centered k-mesh was 6 × 6 × 6 k points mesh. The energy change ΔE_{apb} of the system after the introduction of anti-phase boundary was determined by Equation (4).

$$\Delta E_{apb} = \left(E_{apb} - E_0\right)/2 \tag{4}$$

where, E_0 for the total energy of complete crystal, and E_{apb} for the total energy of crystals with anti-phase boundary. The γ_{apb} was determined by Equation (5).

$$\gamma_{apb} = \Delta E_{apb}/\Delta S \tag{5}$$

where, ΔS for the area of anti-phase boundary.

Supporting Information

Supporting Information is available from the Wiley Online Library or from the author.

Acknowledgements

Q.C., S.T., and W.Z. contributed equally to this work. The authors acknowledge the support from the National Key R&D Program of China (2017YFB0305000), the National Natural Science Foundation of China (52175293 and 51774083), the Reviving-Liaoning Excellence Plan (XLYC1902034), the Central Guidance on Local Science and Technology Development Fund of Liaoning Province (2022JH6/100100062), the Natural Science Foundation of the Jiangsu Higher Education Institutions of China (24KJB430021), and the project funded by the China Postdoctoral Science Foundation (2023M730512). The authors also acknowledge Yu Dong in the Analytical and Testing Center of Northeastern University for the assistance with TEM analysis, and Long Zhang in Shi-changxu Innovation Center for Advanced Materials, Institute of Metal Research, Chinese Academy of Sciences for the analysis of precipitation evolution.

Conflict of Interest

The authors declare no conflict of interest.

Data Availability Statement

The data that support the findings of this study are available from the corresponding author upon reasonable request.

Keywords

cryogenic steels, high impact toughness, high strength, Mo-rich B2 phase, nano-precipitate

Received: August 6, 2024
Revised: September 14, 2024
Published online:

[1] B. Fultz, J. W. Morris, *Metall. Trans. A* **1985**, *16*, 2251.
[2] C. C. Kinney, K. R. Pytlewski, A. G. Khachaturyan, J. W. Morris Jr., *Acta Mater.* **2014**, *69*, 372.
[3] D. Nakanishi, T. Kawabata, S. Aihara, *Mater. Sci. Eng. A* **2018**, *723*, 238.
[4] R. O. Ritchie, *Nat. Mater.* **2011**, *10*, 817.
[5] L. Å. Norström, O. Vingsbo, *Metal Sci.* **1979**, *13*, 677.
[6] W. X. Zhang, Y. Z. Chen, Y. B. Cong, Y. H. Liu, F. Liu, *J. Mater. Sci.* **2021**, *56*, 12539.
[7] E. Hanova, *Weld. Int.* **1991**, *5*, 995.
[8] S. H. Jiang, H. Wang, Y. Wu, X. J. Liu, H. H. Chen, M. J. Yao, B. Gault, D. Ponge, D. Raabe, A. Hirata, M. W. Chen, Y. D. Wang, Z. P. Lu, *Nature* **2017**, *544*, 460.
[9] R. D. Noebe, R. R. Bowman, M. V. Nathal, *Int. Mater. Rev.* **1993**, *38*, 193.
[10] H. Xing, A. P. Dong, J. Huang, J. Zhang, B. D. Sun, *J. Mater. Sci. Technol.* **2018**, *34*, 620.
[11] D. Blavette, E. Cadel, A. Fraczkiewicz, A. Menand, *Science* **1999**, *286*, 2317.
[12] G. D. W. Smith, D. Hudson, P. D. Styman, C. A. Williams, *Philos. Mag.* **2013**, *93*, 3726.
[13] S. Hirosawa, Y. Oguri, T. Sato, *Mater. Trans.* **2005**, *46*, 1230.
[14] Y. Q. Chen, S. P. Pan, S. W. Tang, W. H. Liu, C. P. Tang, F. Y. Xu, *J. Mater. Sci.* **2016**, *51*, 7780.
[15] M. Ogura, T. Fukushima, R. Zeller, P. H. Dederichs, *J. Alloy. Compd.* **2017**, *715*, 454.
[16] N. Abdoshahi, P. Spoerk-Erdely, M. Friák, S. Mayer, M. Šob, D. Holec, *Phys. Rev. Mater.* **2020**, *4*, 103604.
[17] H. I. Aaronson, F. K. LeGoues, *Metall. Trans. A* **1992**, *23*, 1915.
[18] D. Fan, L. Q. Chen, *Acta Mater.* **1997**, *45*, 3297.
[19] J. H. Gao, S. H. Jiang, H. R. Zhang, Y. H. Huang, D. K. Guan, Y. D. Xu, S. K. Guan, L. A. Bendersky, A. V. Davydov, Y. Wu, H. H. Zhu, Y. D. Wang, Z. P. Lu, W. M. Rainforth, *Nature* **2021**, *590*, 262.
[20] J. R. Strife, D. E. Passoja, *Metall. Trans. A* **1980**, *11*, 1341.
[21] B. W. Whitaker, *Fe-12Ni-4Co-2Mo-.05Ti Alloy for use at 77°K and Below*, LBL Publications, Berkeley, CA, USA **1975**.
[22] M. Niikura, J. W. Morris, *Metall. Trans. A* **1980**, *11*, 1531.
[23] J. W. Morris, *The Design of Tough Ferritic Steels for Cryogenic use*, LBL Publications, Berkeley, CA, USA **1985**.
[24] H. S. Shin, H. M. Lee, M. S. Kim, *Int. J. Impact Eng.* **2000**, *24*, 571.
[25] H. K. D. H. Bhadeshia, *Prog. Mater. Sci.* **2012**, *57*, 268.
[26] C. R. Anoop, R. K. Singh, R. R. Kumar, M. Jayalakshmi, T. A. Prabhu, K. T. Tharian, S. V. S. N. Murty, *Mater. Perform. Charact.* **2021**, *10*, 16.
[27] J. Lee, S. S. Sohn, S. Hong, B. C. Suh, S. K. Kim, B. J. Lee, N. J. Kim, S. Lee, *Metall. Mater. Trans. A* **2014**, *45*, 5419.
[28] S. S. Sohn, S. Hong, J. Lee, B. C. Suh, S. K. Kim, B. J. Lee, N. J. Kim, S. Lee, *Acta Mater.* **2015**, *100*, 39.
[29] C. S. Zheng, W. W. Yu, *Mater. Sci. Eng. A* **2018**, *710*, 359.
[30] I. P. Semenova, J. Modina, A. V. Polyakov, G. V. Klevtsov, N. A. Klevtsova, I. N. Pigaleva, R. Z. Valiev, *Mater. Sci. Eng. A* **2019**, *743*, 581.
[31] D. Y. Li, Y. Zhang, *Intermetallics* **2016**, *70*, 24.
[32] M. X. Yang, L. L. Zhou, C. Wang, P. Jiang, F. P. Yuan, E. Ma, X. L. Wu, *Scripta Mater.* **2019**, *172*, 66.
[33] W. F. Gale, T. C. Totemeier, *Smithells metals reference book*, Butterworth-Heinemann, London, UK **2003**.
[34] G. Hettich, H. Mehrer, K. Maier, *Scripta Metall.* **1977**, *11*, 795.
[35] H. Nitta, T. Yamamoto, R. Kanno, K. Takasawa, T. Iida, Y. Yamazaki, S. Ogu, Y. Iijima, *Acta Mater.* **2002**, *50*, 4117.
[36] R. P. Zhang, S. T. Zhao, J. Ding, Y. Chong, T. Jia, C. Ophus, M. Asta, R. O. Ritchie, A. M. Minor, *Nature* **2020**, *581*, 283.
[37] T. W. Xu, S. S. Zhang, S. Liang, N. Cui, L. Cao, Y. Wan, *Sci. Rep.* **2019**, *9*, 17628.
[38] Y. F. Xu, D. Q. Yi, H. Q. Liu, B. Wang, F. L. Yang, *Mater. Sci. Eng. A* **2011**, *529*, 326.
[39] M. Kapoor, D. Isheim, G. Ghosh, S. Vaynman, M. E. Fine, Y. W. Chung, *Acta Mater.* **2014**, *73*, 56.
[40] Z. K. Teng, C. T. Liu, G. Ghosh, P. K. Liaw, M. E. Fine, *Intermetallics* **2010**, *18*, 1437.
[41] A. Keyhani, R. Roumina, S. Mohammadi, *Comp. Mater. Sci.* **2016**, *122*, 281.
[42] A. J. Ardell, *Metall. Trans. A* **1985**, *16*, 2131.
[43] T. Gladman, *Mater. Sci. Technol.* **1999**, *15*, 30.
[44] P. M. Kelly, *Int. Metall. Rev.* **1973**, *18*, 31.
[45] Z. P. Xiong, I. Timokhina, E. Pereloma, *Prog. Mater. Sci.* **2021**, *118*, 100764.
[46] K. I. Sugimoto, N. Usui, M. Kobayashi, S. I. Hashimoto, *ISIJ Int.* **1992**, *32*, 1311.
[47] B. Johansson, L. Vitos, P. A. Korzhavyi, *Solid State Sci.* **2003**, *5*, 931.
[48] L. Vitos, *Phys. Rev. B* **2001**, *64*, 167.
[49] L. Vitos, I. A. Abrikosov, B. Johansson, *Phys. Rev. Lett.* **2001**, *87*, 156401.
[50] L. Vitos, J. O. Nilsson, B. Johansson, *Acta Mater.* **2006**, *54*, 3821.
[51] J. P. Perdew, K. Burke, M. Ernzerhof, *Phys. Rev. Lett.* **1998**, *80*, 891.
[52] G. Kresse, J. Furthmüller, *Phys. Rev. B* **1996**, *54*, 11169.
[53] P. E. Blöchl, *Phys. Rev. B* **1994**, *50*, 17953.
[54] J. P. Perdew, K. Burke, M. Ernzerhof, *Phys. Rev. Lett.* **1996**, *77*, 3865.
[55] Y. H. Zhao, *Intermetallics* **2022**, *144*, 107528.
[56] V. R. Manga, S. L. Shang, W. Y. Wang, Y. Wang, J. Liang, V. H. Crespi, Z. K. Liu, *Acta Mater.* **2015**, *82*, 287.